

The infrared dust bubble N22: an expanding H II region and the star formation around it

Wei-Guang Ji^{1,2}, Jian-Jun Zhou^{1,3}, Jarken Esimbek^{1,3}, Yue-Fang Wu⁴, Gang Wu^{1,3}, and
Xin-Di Tang^{1,2}

¹ Xinjiang Astronomical Observatory, Chinese Academy of Sciences, Urumqi 830011, PR China
e-mail: jiweiguang@xao.ac.cn

² Graduate University of the Chinese Academy of Sciences, Beijing 100080, PR China

³ Key Laboratory of Radio Astronomy, Chinese Academy of Sciences, Urumqi 830011, PR China

⁴ Department of Astronomy, Peking University, 100871, Beijing China

Accepted 30/05/2012

ABSTRACT

Aims. To increase the observational samples of star formation around expanding H II regions, we analyzed the interstellar medium and star formation around N22.

Methods. We used data extracted from the seven large-scale surveys from infrared to radio wavelengths. In addition we used the JCMT* observations of the $J = 3-2$ line of ^{12}CO emission data released on CADC** and the ^{12}CO $J = 2-1$ and $J = 3-2$ lines observed by the KOSMA*** 3 m telescope. We performed a multiwavelength study of bubble N22.

Results. A molecular shell composed of several clumps agrees very well with the border of N22, suggesting that its expansion is collecting the surrounding material. The high integrated ^{12}CO line intensity ratio $R_{\text{CO}(3-2)/\text{CO}(2-1)}$ (ranging from 0.7 to 1.14) implies that shocks have driven into the molecular clouds. We identify eleven possible O-type stars inside the H II region, five of which are located in projection inside the cavity of the 20 cm radio continuum emission and are probably the exciting-star candidates of N22. Twenty-nine YSOs (young stellar objects) are distributed close to the dense cores of N22. We conclude that star formation is indeed active around N22; the formation of most of YSOs may have been triggered by the expanding of the H II region. After comparing the dynamical age of N22 and the fragmentation time of the molecular shell, we suggest that radiation-driven compression of pre-existing dense clumps may be ongoing.

Key words. ISM: H II regions - ISM: clouds - stars: formation

1. Introduction

Using the Spitzer-GLIMPSE¹ survey of the Galactic plane (Benjamin et al. 2003), Churchwell et al. (2006, 2007) cataloged almost 600 infrared (IR) dust bubbles. The IR dust bubbles are bordered

* James Clerk Maxwell Telescope <http://www.jach.hawaii.edu/JCMT/>

** The Canadian Astronomy Data Centre <http://www3.cadc-ccda.hia-ihp.nrc-cnrc.gc.ca/>

*** KOSMA <http://www.astro.uni-koeln.de/kosma/>

¹ Galactic Legacy Infrared Mid-Plane Survey Extraordinaire

<http://irsa.ipac.caltech.edu/data/SPITZER/GLIMPSE/>

Please give a shorter version with: \authorrunning and/or \titilerunning prior to \maketitle

by bright 8 μm shells (the photo-dissociation region (PDR)) that encloses bright 24 μm interiors. Of these IR dust bubbles, Deharveng et al. (2010) have studied a series of 102 ionized bubbles and concluded that 86 % of these bubbles enclose H II regions.

Deharveng et al. (2010) also concluded that star formation triggered by H II regions may be an important process, especially for massive-star formation. Elmegreen (1998) and Deharveng et al. (2005) proposed various physical mechanisms of triggered the formation of stars around the H II regions. Recently, one of the triggered processes called "collect and collapse", proposed by Elmegreen & Lada (1977), has been studied in more detail inside the H II region borders, and several observational studies supported that this mechanism is ongoing in several H II regions (see e.g. Zavagno et al. 2007 & 2010; Pomars et al. 2009; Petriella et al. 2010).

N22 is one of the northern IR dust bubbles cataloged by Churchwell et al. (2006). By checking the infrared (8 and 24 μm) image and the JCMT $^{12}\text{CO } J = 3-2$ data of N22, we found collected material, which indicates that triggered star formation may be taking place around N22. In this work, we present a molecular and IR study of the environment surrounding the IR dust bubble N22 to explore its surrounding ISM and search for signatures of star formation. We describe our data in Sect. 2, present N22 in Sect. 3, and the molecular analysis in Sect. 4 along with the exciting star(s) and star formation, Sect. 5 details our analysis of the star formation mechanism, and we summarize our findings in Sect.6.

2. Data

Seven large-scale surveys were used in our study: 2MASS², GLIMPSE, MIPS GAL³, NVSS⁴, GRS⁵, AKARI-BSC⁶, and the BGPS⁷ catalog.

The GLIMPSE and MIPS GAL (Carey et al. 2005) surveys were performed using the *Spitzer* Space Telescope (Werner et al. 2004). We used the mosaicked images from GLIMPSE and MIPS GAL acquired by *Spitzer*-IRAC (3.6, 4.5, 5.8 and 8 μm) (Fazio et al. 2004) and the MIPS instrument (24 and 70 μm) (Rieke et al. 2004), respectively. IRAC has an angular resolution of between 1.''5 and 1.''9. The MIPS GAL resolution at 24 μm is 6''. The four far-infrared wavelengths of AKARI are centered at 65, 90, 140, and 160 μm , and their angular resolutions are 26.''8, 26.''8, 44.''2 and 44.''2, respectively (Murakami et al. 2007). The BGPS is a 1.1mm continuum survey with an angular resolution of 33'' (Aguirre et al. 2011). We also used the GLIMPSE Point-Source Catalog (GPSC), AKARI-BSC (Yamamura et al. 2010), and the BGPS catalog (Rosolowsky et al. 2010).

In addition, we used the 1.4 GHz radio continuum emission data extracted from the NVSS with an angular resolution of about 45'' (Condon et al. 1998). For the molecular analysis, we used the James Clerk Maxwell Telescope (JCMT) observations of the $J = 3-2$ line of ^{12}CO emission data released on CADC and the $^{13}\text{CO } J = 1-0$ from GRS performed by the Boston University and the

² Two Micron All Sky Survey <http://pegasus.phast.umass.edu/>

³ MIPS GAL <http://irsa.ipac.caltech.edu/data/SPITZER/MIPSGAL/>

⁴ NRAO VLA Sky Survey <http://www.cv.nrao.edu/nvss/>

⁵ Galactic Ring Survey http://www.bu.edu/galacticring/new_index.htm

⁶ Far-Infrared Survey (FIS) for AKARI Bright Source Catalog

<http://heasarc.gsfc.nasa.gov/W3Browse/all/akaribsc.html>

⁷ The Bolocam Galactic Plane Survey <http://milkyway.colorado.edu/bgps/>

Please give a shorter version with: \authorrunning and/or \titilerunning prior to \maketitle

Five College Radio Astronomy Observatory (FCRAO). The co-added spectral cubes of the JCMT $^{12}\text{CO } J = 3-2$ line were binned to 0.2 km s^{-1} , and the data were smoothed with a $6''$ Gaussian kernel. The final spatial resolution of each cube is $16''$ (Smith et al. 2008), while the angular and spectral resolution of the GRS $^{13}\text{CO } J = 1-0$ are $46''$ and 0.2 km s^{-1} (Jackson et al. 2006).

We observed the $^{12}\text{CO } J = 2-1$ and $J = 3-2$ lines using the KOSMA 3 m telescope at Gornergrat, Switzerland in 2010 February. The half-power beamwidths of the telescope at observing frequencies of 230.538 GHz and 345.789 GHz are $130''$ and $80''$, and their corresponding system temperatures are about 233.5 and 357.8 K. The pointing and tracking accuracy is better than $10''$.

3. Presentation of N22

N22 is a complete IR dust bubble centered on $\alpha_{2000} = 276^{\circ}325$, $\delta_{2000} = -13^{\circ}176$ ($l = 18^{\circ}254$, $b = -0^{\circ}305$) (Churchwell et al. 2006) with a radius of about 1.77 pc (Beaumont & Williams 2010). N22 was also known as an H II region (G18.259 – 0.307) (Kolpak et al. 2003), its hydrogen recombination line velocity v_{LSR} is $\sim 50.9 \text{ km s}^{-1}$. Kolpack and collaborators derived the near distance by comparison with the H I absorption data of G18.259 – 0.307, and obtained kinematic distances of $\sim 4.1 \pm 0.3 \text{ kpc}$. We adopt their v_{LSR} and kinematic distance for N22.

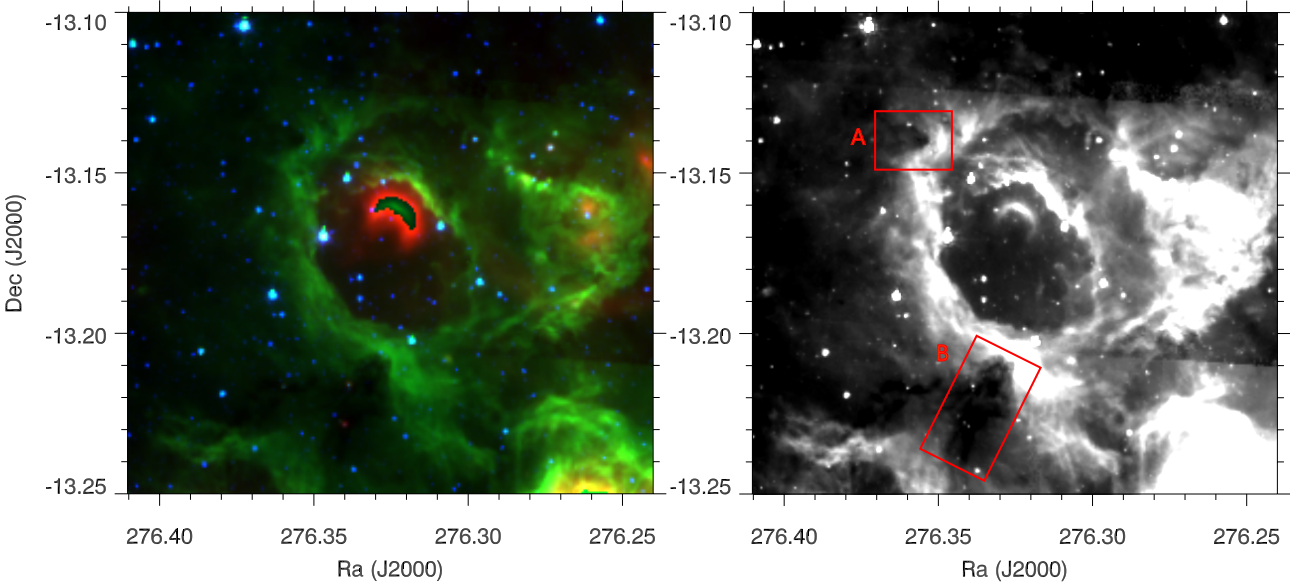


Fig. 1. Left: Mid-IR emission of the IR dust bubble N22: *Spitzer* three-color image ($4.5 \mu\text{m} = \text{blue}$, $8 \mu\text{m} = \text{green}$, and $24 \mu\text{m} = \text{red}$). Right: The background shows the *Spitzer*-IRAC $8 \mu\text{m}$ emission. The two rectangles show the location of two IRDCs, which are named A and B.

Fig. 1 (left) shows a *Spitzer*-IRAC and *Spitzer*-MIPSGAL three-color image of N22 ($4.5 \mu\text{m}$ in blue, $8 \mu\text{m}$ in green, and $24 \mu\text{m}$ in red). The $24 \mu\text{m}$ emission corresponding to hot dust is distributed mainly toward the north of N22 (because of overexposure there are some bad data points in the peak of $24 \mu\text{m}$). The PDR visible in the $8 \mu\text{m}$ emission is generally attributed to polycyclic aromatic hydrocarbon (PAH) molecules. Infrared emission from PAHs is a good tracer of ionization fronts (IF) because these large molecules are believed to be destroyed inside the ionized region, but are excited in the PDR by the radiation leaking from the H II region (Pomars et al. 2009). The absorption in $8 \mu\text{m}$ usually indicates infrared dark clouds (IRDCs). Two absorptions appear in the gray map of

Please give a shorter version with: \authorrunning and/or \titilerunning prior to \maketitle

8 μm (right panel of Fig. 1), they were marked by two red rectangles. Because these two absorptions are bordered by bright 8 μm and the ionization fronts are distorted, we conclude that these two structures are indeed IRDCs (hereafter IRDC-A and IRDC-B). They have not been cataloged in the IRDC catalogs of Simon et al. (2006) and Peretto & Fuller (2009). However, IRDC-B has been identified by Watson et al. (2008) when they studied the nearby infrared dust bubble N21.

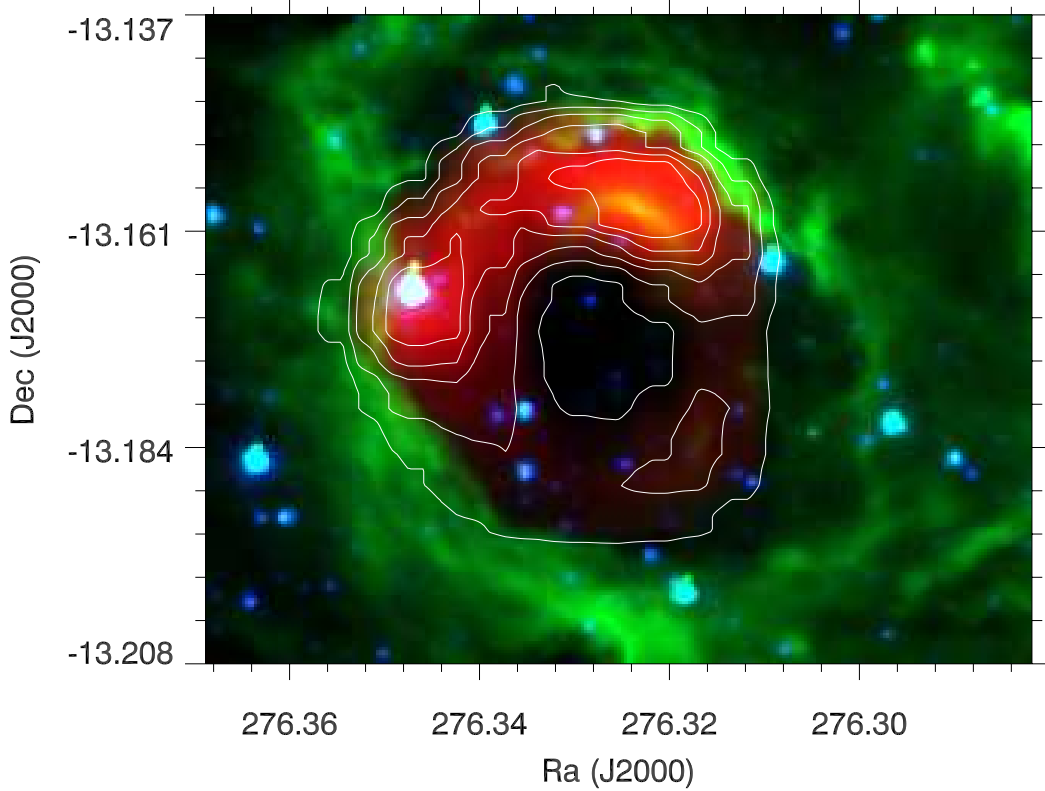


Fig. 2. *Spitzer*-IRAC emission at 4.5 μm (in blue), 8 μm (in green), and the NVSS radio continuum emission at 20 cm (in red and emphasized with white contours). The levels range from 0.05 to 0.15 by 0.02 Jy beam^{-1} . The σ_{rms} of the NVSS data is 0.45 mJy beam^{-1} .

Fig. 2 shows the *Spitzer*-IRAC emission at 4.5 μm (in blue), 8 μm (in green), and the NVSS radio continuum emission at 20 cm (in red and emphasized with white contours). The 20 cm emission, which is commonly attributed to the free-free emission from H II regions, is bounded by 8 μm emission. The 20cm emission shows a shell morphology, and a cavity can be clearly seen at its center. The strong 20 cm emission is distributed in the north of the shell, and shows an arc-like structure. Two peaks appears in the arc, and the stronger one is coincident with a small arc traced by 8 μm emission.

4. Molecular analysis and star formation

4.1. Molecular analysis

We used the $^{12}\text{CO } J = 3-2$ data cube from JCMT to analyze the molecular environment around N22. Fig. 3 shows the integrated velocity channel maps of the $^{12}\text{CO } J = 3-2$ emission from 43.0 to 56.5 km s^{-1} in steps of 1.5 km s^{-1} . Between 49.0 and 55.0 km s^{-1} , several molecular clumps are

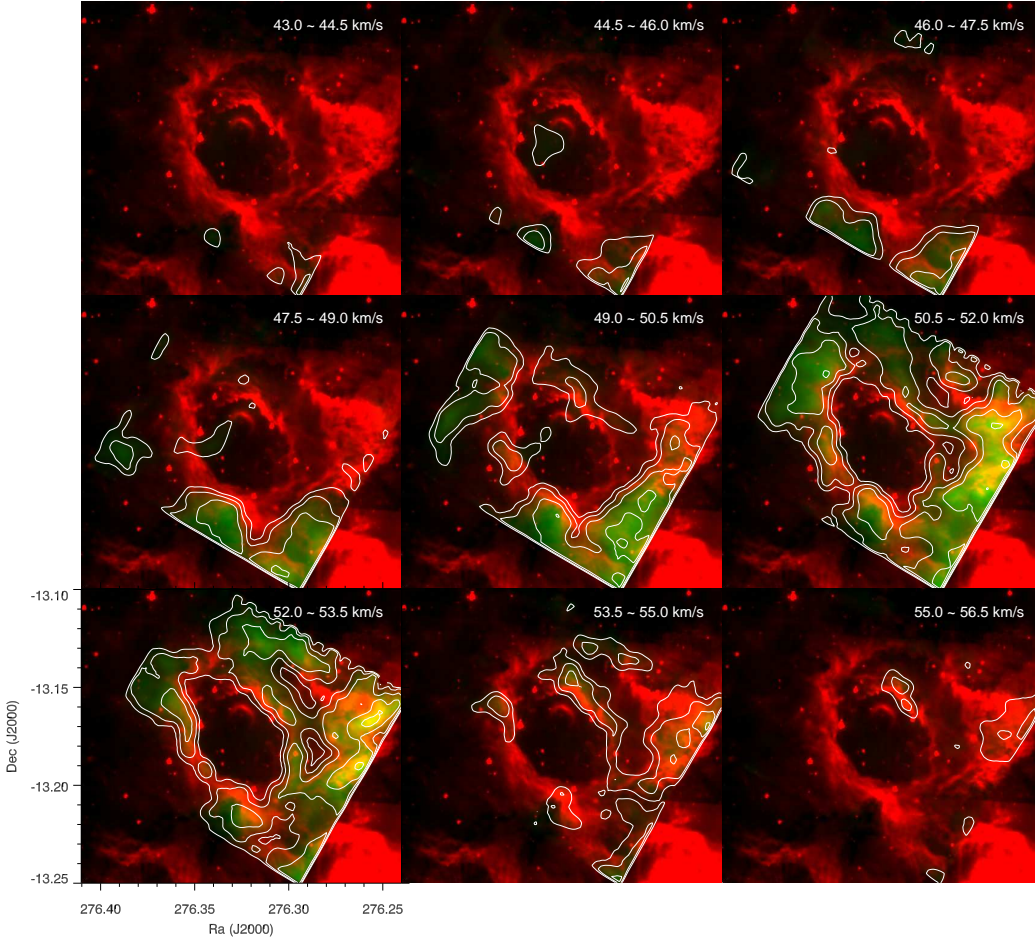


Fig. 3. Integrated velocity channel maps of the JCMT $^{12}\text{CO } J = 3-2$ emission every 1.5 km s^{-1} from 43.0 to 56.5 km s^{-1} (in green) superimposed on the $8 \mu\text{m}$ emission (in red). The contour levels of the $^{12}\text{CO } J = 3-2$ emission are $5, 10, 20, 35,$ and 55 K km s^{-1} . The angular resolution of the JCMT $^{12}\text{CO } J = 3-2$ emission is $16''$.

distributed across the border of N22, which may indicate where the collect-and-collapse process could be taking place.

We integrated the JCMT $^{12}\text{CO } J = 3-2$ emission between 40 and 60 km s^{-1} (in green) over the $8 \mu\text{m}$ emission (in red) (see Fig. 4). Molecular cores 1-11 are clearly identifiable and are indeed distributed across the borders of N22, which as pointed out by Deharveng et al. (2005), may be indicative of the collect-and-collapse mechanism.

From Fig.1 (right) and Fig.4, we can see that the molecular cores 1 and 4 are associated with IRDC-A and IRDC-B. These two IRDCs distort the IF excited at the $8 \mu\text{m}$, which are presently compressed by the ionized gas. They may have preexisted there before the HII region expanded to reach them. This is consistent with the model "radiation-driven compression" (Deharveng et al. 2010). Based on the analysis above, we conclude that IRDC-B is physically associated with N22, and so is IRDC-A.

Assuming local thermodynamical equilibrium for the gas and an optically thick condition for the $^{12}\text{CO } J = 3-2$ line, we estimated the excitation temperature of the $^{12}\text{CO } J = 3-2$ line following the equation $T_{\text{ex}} = 16.6 / \ln [1 + 1 / (T_{\text{mb}} / 16.6 + 0.0024)]$ (Buckle et al. 2010), where T_{mb} is the main-beam temperature. Because it is difficult to obtain the optical depth τ from one transition of

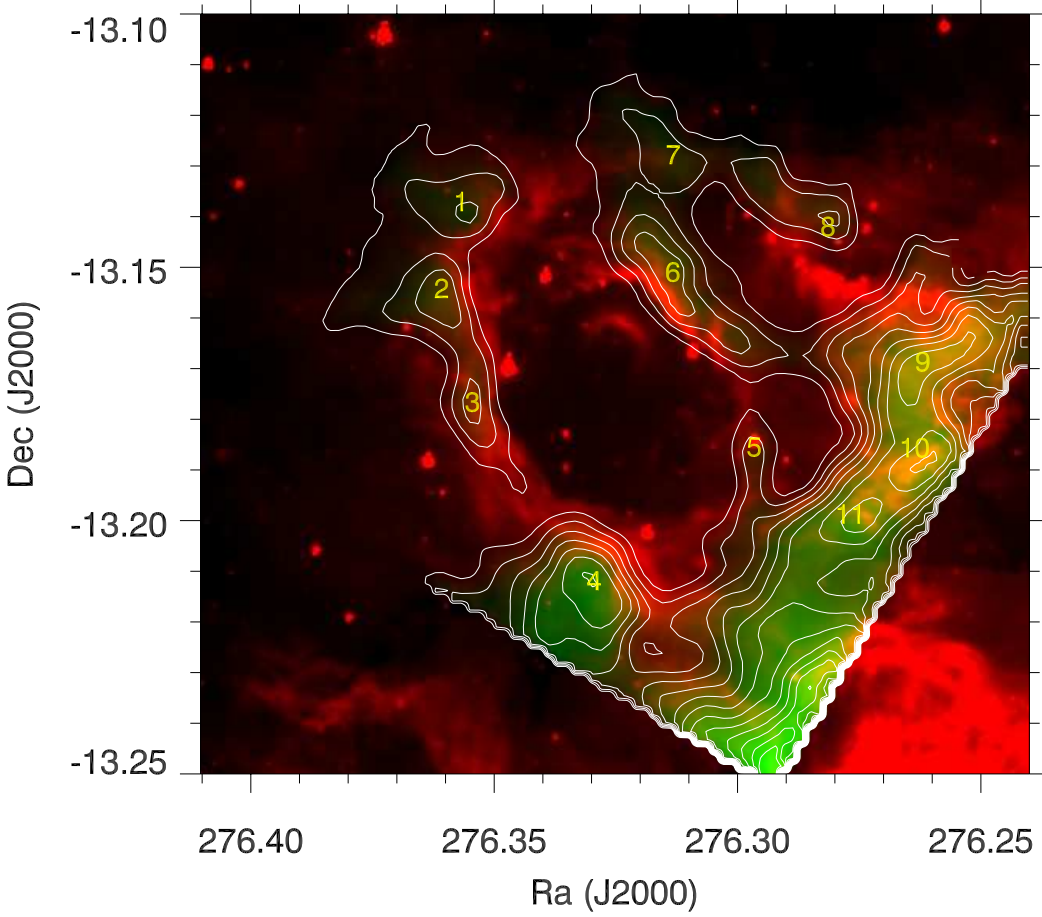


Fig. 4. JCMT $^{12}\text{CO } J = 3-2$ emission (in green) integrated between 40 and 60 km s^{-1} . The contour levels of the $^{12}\text{CO } J = 3-2$ emission increase from 50.0 to 252.9 by 16.9 K km s^{-1} . Red is the $8 \mu\text{m}$ emission. The yellow numbers are the ID of molecular cores.

CO, we used the X factor between H_2 and ^{12}CO to estimate the column density of the 11 molecular cores. According to Shetty et al. (2011), the X factor is $\sim 1 - 6 \times 10^{20} \text{ cm}^{-2} \text{ K}^{-1} \text{ km}^{-1} \text{ s}$. Here we assume $X = 6 \times 10^{20} \text{ cm}^{-2} \text{ K}^{-1} \text{ km}^{-1} \text{ s}$ and estimated the column density using the formula

$$N_{\text{H}_2} = 6 \times 10^{20} W_{\text{CO}} [\text{cm}^{-2}],$$

where W_{CO} is the observed ^{12}CO intensity, estimated following the equation $W_{\text{CO}} = \int T_{\text{mb}} dv \text{ cm}^{-2} \text{ K km s}^{-1}$. If the cloud cores are approximately spherical in shape, the mean H_2 number density is $n_{\text{H}_2} = 1.62 \times 10^{-19} N_{\text{H}_2} / L$, where L is the cloud core diameter in parsecs (pc). The mass is given by $M_{\text{H}_2} = 1.13 \times 10^{-4} \mu_{\text{g}} m(\text{H}_2) D^2 S N_{\text{H}_2} [M_{\odot}]$ (Buckle et al. 2010), where D is the distance in pc, S is the pixel area in arcsec^2 , $\mu_{\text{g}} = 1.36$ is the mean atomic weight of the gas, and $m(\text{H}_2)$ is the mass of a hydrogen molecule. Finally, we list L , T_{ex} , N_{H_2} , M_{H_2} , and n_{H_2} of molecule cores 1 ~ 11 in Cols. 5-9 of Table 1, respectively. We used Gaussian fittings to obtain the peak temperature, velocity width, and central velocity. They are listed in Cols. 2-4 of Table 1.

Fig. 5 displays spectra at the peak of the molecule cores 1-11, the JCMT $^{12}\text{CO } J = 3-2$ spectra and GRS $^{13}\text{CO } J = 1-0$ spectra enlarged three times are depicted in black and red. The $^{12}\text{CO } J = 3-2$ spectra of #2, #4, #6, and #11 seem to show self-absorption, but corresponding $^{13}\text{CO } J = 1-0$ show no evidence of self-absorption. Taking into consider the integrated velocity channel maps (see Fig. 3), we suggest that $^{12}\text{CO } J = 3-2$ spectra of #2, #4, #6, and #11 include some different

Please give a shorter version with: \authorrunning and/or \titilerunning prior to \maketitle

Table 1. The parameters of the molecular cores 1-11

core	peak temperature (K)	central velocity (km s ⁻¹)	velocity width (km s ⁻¹)	L (pc)	T_{ex} (K)	N_{H_2} (10 ²² cm ⁻²)	M_{H_2} (10 ³ M_{\odot})	n_{H_2} (10 ³ cm ⁻³)
1	20.97	51.28	2.32	1.78	28.50	3.11	1.70	2.83
2	20.15	51.43	2.34	1.49	27.66	3.01	1.15	3.28
3	15.79	50.49	1.48	1.18	23.14	1.49	0.36	2.04
4	20.69	48.65	3.03	1.86	28.21	4.01	2.38	3.49
5	11.27	52.73	1.86	0.88	18.37	1.34	0.18	2.47
6	10.54	53.83	4.24	1.47	17.59	2.86	1.06	3.14
7	19.37	52.56	1.96	1.73	26.86	2.42	1.25	2.27
8	23.17	51.75	1.96	1.29	30.76	2.90	0.82	3.65
9	26.32	51.76	3.00	1.73	33.99	5.05	2.59	4.73
10	39.77	51.81	3.40	1.18	47.63	8.64	2.08	11.85
11	30.45	51.74	3.41	1.46	38.19	6.63	2.44	7.35

Notes. Comparing the spectra between ¹²CO $J = 2-1$ and ¹³CO $J = 1-0$ and channel maps of ¹²CO $J = 2-1$, we suggest that the dips in the ¹²CO 3-2 profiles of molecular cores #2, #4, #6, and #11 do not indicate self-absorption. Here we just consider the spectra main component associated to each clump of N22.

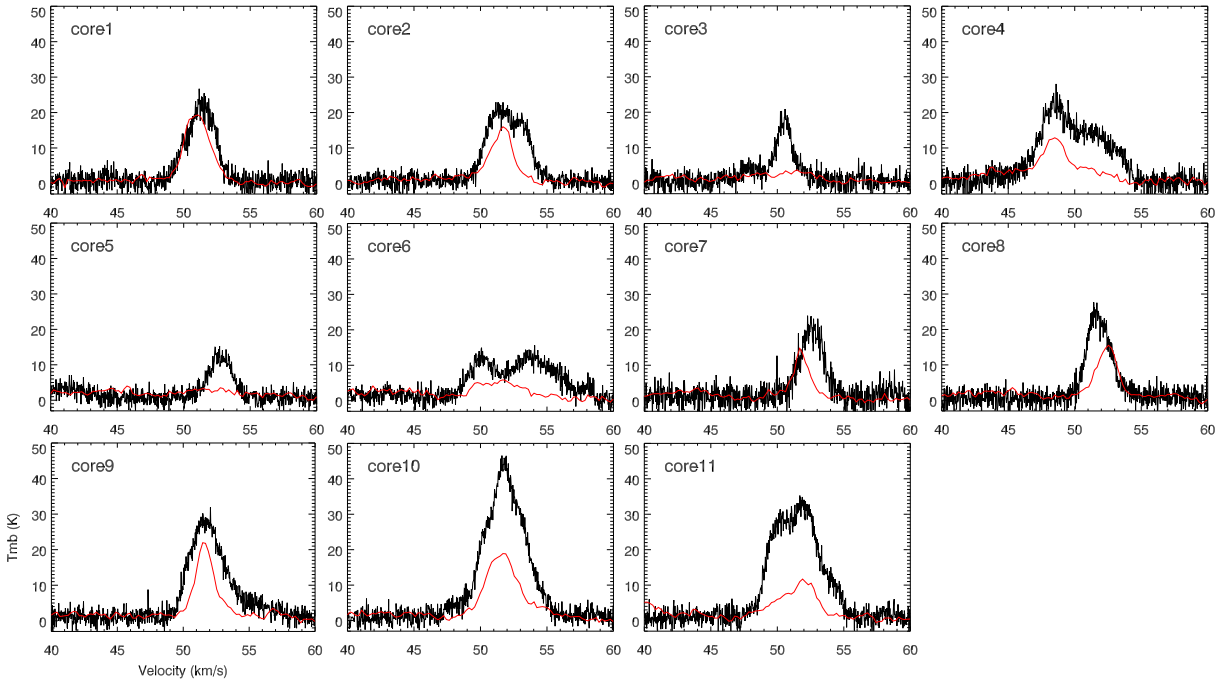


Fig. 5. JCMT ¹²CO $J = 3-2$ spectra at the peak of cores 1-11 are given in black, and GRS ¹³CO $J = 1-0$ spectra enlarged three times at the same region are delineated in red.

velocity components. Here we just consider the spectra main component associated to each clump of N22, which is centered at the velocity quoted in Table 1.

4.2. The expanding HII region interacting with its surrounding material

As mentioned above, the morphology of N22 strongly suggests that the observed molecular shell has been swept and shaped by the expansion of N22 (see Fig. 4). The different transitions of ¹²CO

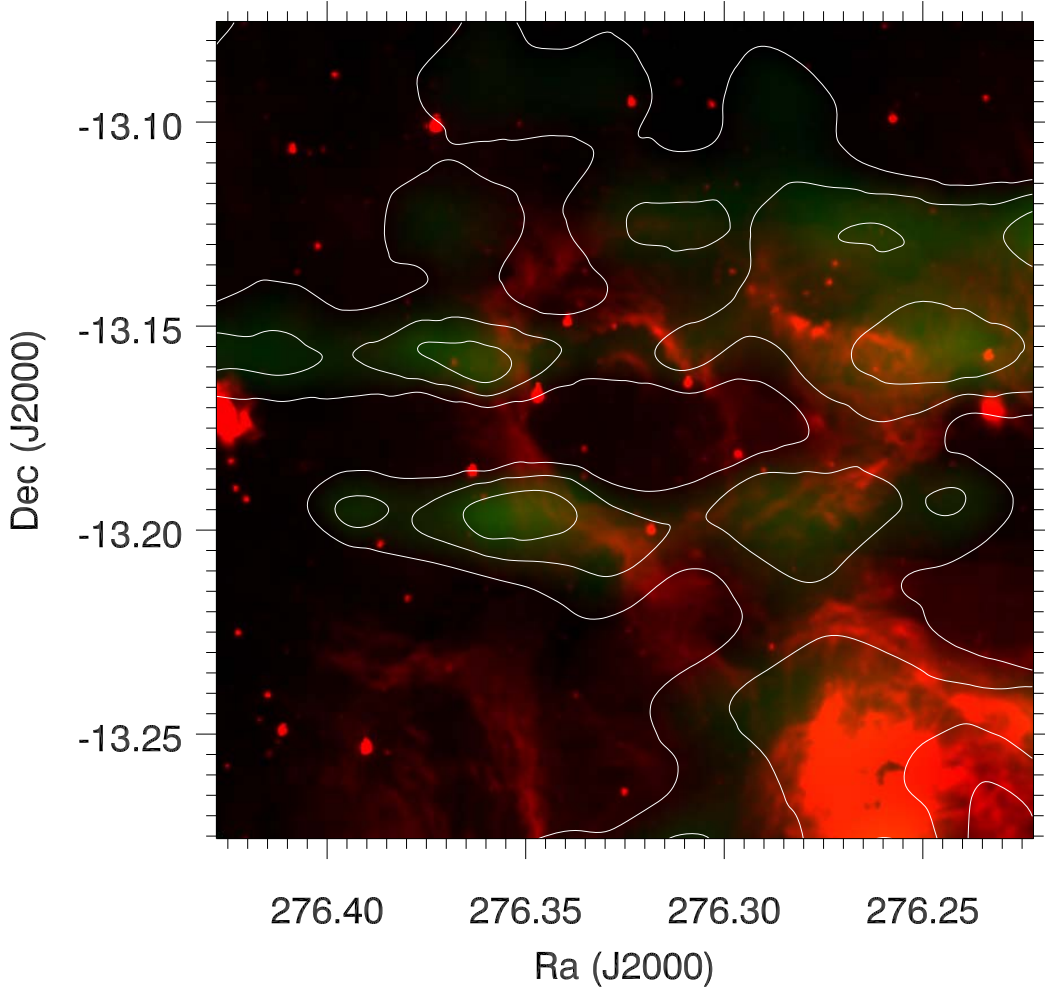


Fig. 6. Line intensity ratios $R_{I_{CO(3-2)}/I_{CO(2-1)}}$ from KOSMA $^{12}\text{CO } J = 3-2$ and $^{12}\text{CO } J = 2-1$ is given in green, which is superimposed on the $8 \mu\text{m}$ emission in red. The contours range from 0.72 to 1.14 by 0.14.

can trace different molecular environments. To obtain the integrated intensity ratio of $^{12}\text{CO } J = 3-2$ to $^{12}\text{CO } J = 2-1$ ($R_{I_{CO(3-2)}/I_{CO(2-1)}}$), we convolved the $^{12}\text{CO } J = 3-2$ data to the same angular resolution as for $^{12}\text{CO } J = 2-1$. We performed an integrated ^{12}CO line intensity ratio $R_{I_{CO(3-2)}/I_{CO(2-1)}}$ for the whole bubble using the KOSMA data, which is between 0.7 and 1.14 (see Fig. 6). The ratios around N22 are higher than 0.8, which is much higher than previous measurements of individual Galactic Molecular Clouds (MCs) (0.55, Sanders et al. 1993) and even higher than the value (0.8) in the starburst galaxies M82 (Guesten et al. 1993). The higher line ratios imply that shocks have driven into the MCs (Xu et al. 2011). Hereafter, the regions with higher line ratios (> 0.8) are called "the active regions". Our result indicates that the expanding H II region is interacting with its surrounding material.

4.3. Exciting stars

No exciting stars of N22 have been described in the literature. However, according to the 20 cm flux and the estimated ionizing photon rate of N22, Beaumont & Williams (2010) stated that at least ten O9.5 stars are needed to produce the observed radio flux. To search for the exciting stars,

Table 2. Exciting star candidates inside the H II region

#	GLIMPSE Desig.	J	H	K_s	A_V	M_J	M_H	M_{K_s}	O-type star
1	G018.2516-00.3068	12.20	11.04	10.56	10.50	-3.83	-3.86	-3.68	O8V-O7V
2	G018.2714-00.3026	12.18	9.50	8.18	24.29	-7.73	-7.81	-7.60	–
3	G018.2443-00.3096	11.14	9.62	8.94	13.85	-5.83	-5.87	-5.68	–
4	G018.2518-00.3097	14.49	12.05	10.97	21.30	-4.58	-4.74	-4.48	O5.5V-O4V
5	G018.2668-00.2907	13.01	11.42	10.68	14.61	-4.17	-4.21	-4.02	O7V-O6V
6	G018.2496-00.2955	13.60	12.25	11.65	12.40	-2.96	-2.99	-2.81	–
7	G018.2559-00.3008	16.16	13.27	12.00	24.91	-3.93	-4.15	-3.86	O7.5V-O6V
8	G018.2618-00.3044	13.93	11.10	9.81	24.75	-6.12	-6.30	-6.03	–
9	G018.2627-00.3137	16.04	13.21	11.94	24.64	-3.97	-4.16	-3.89	O7.5V-O6V
10	G018.2532-00.3059	14.27	11.82	10.72	21.46	-4.85	-5.00	-4.75	O5V-O3V
11	G018.2660-00.2987	10.30	9.77	9.47	6.12	-4.50	-4.36	-4.28	O6V-O5V
12	G018.2680-00.3114	14.75	12.96	12.12	16.38	-2.93	-2.97	-2.78	–
13	G018.2521-00.3020	12.07	10.95	10.40	10.87	-4.06	-4.02	-3.88	O7V-O6.5V
14	G018.2441-00.2966	16.06	12.26	10.47	33.30	-6.40	-6.63	-6.33	–
15	G018.2531-00.2907	12.69	11.50	11.06	10.32	-3.29	-3.37	-3.16	–
16	G018.2380-00.3001	13.53	11.13	9.92	22.07	-5.77	-5.80	-5.62	–
17	G018.2431-00.3158	13.87	12.37	11.57	14.63	-3.32	-3.26	-3.13	–
18	G018.2456-00.3205	12.38	10.98	10.35	12.82	-4.30	-4.33	-4.15	O6.5V-O5.5V
19	G018.2365-00.2990	16.04	12.07	9.99	36.36	-7.28	-7.35	-7.14	–
20	G018.2366-00.3083	14.67	12.06	10.88	22.80	-4.83	-5.00	-4.73	O5V-O3V
21	G018.2412-00.3181	10.19	9.58	9.39	5.68	-4.47	-4.48	-4.31	O6V-O5V
22	G018.2455-00.3170	14.37	11.78	10.52	23.45	-5.31	-5.39	-5.17	–
23	G018.2520-00.3115	13.93	12.49	11.86	13.01	-2.80	-2.85	-2.66	–

Notes. The numbers of the sources correspond to the numeration in Fig. 7.

we performed a photometric study of the infrared point sources inside the H II region based on the GLIMPSE I Spring’07 and the 2MASS All-Sky Point Source Catalogs.

Taking into account that the exciting stars are expected to be in a PAHs hole, we just considered the sources inside the H II region. They should be detected in the four *Spitzer*-IRAC bands and three 2MASS bands. Finally, we found 24 sources. Following the color criteria of Allen et al. (2004), we found 23 main-sequence (Class III) stars (see Fig. 7). Most of them are located inside the H II region where the 20 cm radio continuum emission is weak.

To search for O-type stars, we used the J , H , and K apparent magnitudes obtained from the 2MASS Point Source Catalog to derive the absolute JHK magnitudes. We assumed a distance of 4.1 kpc and obtained the extinction for each source from the $(J-H)$ vs. $(H-K)$ color-color diagram. We also assumed the interstellar reddening law of Rieke & Lebofsky (1985) ($A_J/A_V=0.282$; $A_H/A_V=0.175$ and $A_K/A_V=0.112$) and the intrinsic colors $(J-H)_0$ and $(H-K)_0$ obtained from Martins & Plez (2006). By comparing the derived absolute JHK magnitudes with those tabulated by Martins & Plez (2006), we found 11 O-type stars inside the H II region, these are #1, #4, #5, #7, #9, #10, #11, #13, #19, #21, and #22. Table 2 presents these sources with their 2MASS designation (Col. 2), apparent JHK magnitudes (Cols. 3-5), estimated extinctions (Col. 6), calculated absolute JHK magnitudes (Cols. 7-9), and indicates whether their derived spectral type coincides with an O-type in Col. 10.

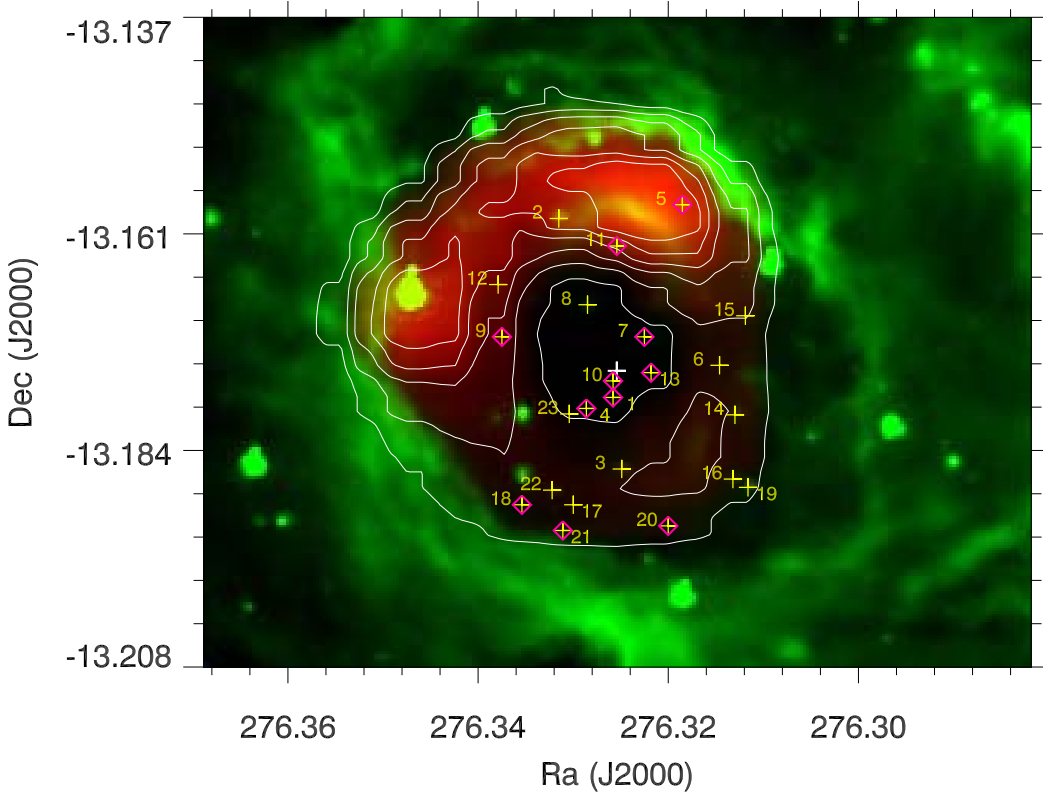


Fig. 7. Two color image, 8 μm in red and 20 cm in green with contours, which are similar to Fig. 2. The yellow plus show the location of the main sequence stars inside the H II region. The red diamonds are the O-type stars. The white plus is the center of N22.

Owing to the proper motion of ionizing star(s), they are not always located in the geometrical center of the H II region. But because of the young ages of the IR dust bubble, the ionizing star(s) may be located near the geometrical center and still lie inside the cavity created by stellar wind. We can see that five O-type stars, #1, #4, #7, #10, and #13, are located in projection inside the cavity of the 20 cm radio continuum emission (see Fig. 7), they are probably the exciting stars of N22.

4.4. SED fitting and star formation

Our analysis suggests that triggered star formation may take place around N22. To search for YSO candidates within a circle of 4.5 in radius centered at N22, we constructed a color-color diagram [5.8]-[8.0] versus [3.6]-[4.5] with the sources that have fluxes in the four *Spitzer*-IRAC bands. We used the photometric criteria of Allen et al. (2004) and the color criterion $m_{4.5} - m_{8.0} > 1$ (Robitaille et al. 2008) to identify class I and II YSOs (see Fig. 8). Finally, we selected 32 sources around N22 (see Fig. 9) and 10 of them, YSO-3, 4, 6, 9, 15, 19, 22, 24, 25, and 30, are cataloged by Robitaille et al. (2008) as Galactic midplane *Spitzer* red sources. Robitaille et al. (2008) pointed out that at most 0.4 % of the intrinsically red sources selected by the color criterion $m_{4.5} - m_{8.0} > 1$ are galaxies and AGNs. Hence, there is a low probability of finding an extragalactic source in our small sample.

The contributions from the disk and envelope of YSOs in the spectral energy distribution (SED) usually comes from long wavelengths, which are longer than ~ 10 microns and up to the millimeter region of the electromagnetic spectrum. Therefore longer wavelength data are needed to obtain a reliable SED for a YSO. We used the 'phot' tool of Aladin (Bonnarel et al. 2000) to obtain the

Please give a shorter version with: \authorrunning and/or \titilerunning prior to \maketitle

Table 3. Near- and mid-IR fluxes of the 32 sources satisfying the photometric criteria of Allen et al. (2004) and the color criterion of $m_{4.5} - m_{8.0} \geq 1$ around N22

Source	GLIMPSE Desig.	J (mag)	H (mag)	K_S (mag)	$3.6 \mu\text{m}$ (mag)	$4.5 \mu\text{m}$ (mag)	$5.8 \mu\text{m}$ (mag)	$8.0 \mu\text{m}$ (mag)	$24 \mu\text{m}$ (mag)
YSO-1	G018.3251-00.3133	15.206	14.274	13.681	12.331	11.716	11.169	10.524	5.19
YSO-2	G018.3145-00.3141			13.108	11.341	10.993	10.459	9.993	
YSO-3	G018.2351-00.3532	13.427	13.002	12.572	11.090	9.835	8.988	8.330	3.88
YSO-4	G018.1992-00.3520			13.624	11.033	10.017	9.224	8.743	5.15
YSO-5	G018.1997-00.3381		14.356	12.547	11.369	11.112	10.724	10.064	3.00
YSO-6	G018.2262-00.3348				12.367	10.171	8.720	7.806	2.71
YSO-7	G018.2171-00.3426				13.550	11.061	9.845	8.918	
YSO-8	G018.2249-00.3352			12.869	11.573	10.592	9.925	9.405	
YSO-9	G018.2157-00.3419				12.930	10.305	9.258	8.445	
YSO-10	G018.2277-00.3303				12.693	11.712	10.928	10.356	
YSO-11	G018.2149-00.2872				12.555	12.136	10.962	10.172	3.67
YSO-12	G018.1976-00.2720	14.253	13.243	12.064	10.728	10.584	10.037	9.420	3.65
YSO-13	G018.2031-00.2641		14.616	13.578	11.920	11.374	10.729	10.304	
YSO-14	G018.2307-00.2427				10.470	9.884	9.038	8.612	0.92
YSO-15	G018.2318-00.2474			13.321	11.331	10.667	10.049	9.304	0.93
YSO-16	G018.2336-00.2373				10.655	9.827	8.909	8.429	
YSO-17	G018.3058-00.2646				11.841	11.267	10.965	9.960	3.99
YSO-18	G018.2548-00.2441				12.808	11.200	10.534	10.170	3.31
YSO-19	G018.2595-00.2488				13.088	12.392	9.999	8.284	2.80
YSO-20	G018.2710-00.2657	16.190	14.493	13.778	11.499	10.849	10.284	9.601	3.96
YSO-21	G018.2534-00.2492				13.645	11.846	8.622	6.972	2.18
YSO-22	G018.2758-00.2636			12.501	9.470	8.050	6.964	6.279	2.91
YSO-23	G018.2790-00.2652				13.475	11.528	9.935	8.880	5.16
YSO-24	G018.2656-00.2405				10.827	8.850	7.235	6.160	2.97
YSO-25	G018.2939-00.2528			14.025	9.671	8.224	7.351	6.945	4.16
YSO-26	G018.2907-00.2629			13.910	11.870	11.183	10.614	9.913	
YSO-27	G018.2573-00.2506				13.125	11.227	9.054	8.372	2.73
YSO-28	G018.2915-00.2689				13.322	11.806	10.490	9.663	
YSO-29	G018.2311-00.3150				11.914	11.406	10.533	9.611	3.41
YSO-30	G018.2383-00.2910	14.385	13.076	11.883	10.262	9.702	8.984	7.592	
YSO-31	G018.2362-00.3032				13.021	11.723	10.807	9.904	2.76
YSO-32	G018.2755-00.3118				13.188	12.867	10.458	8.923	1.24

Notes. The numbers of the YSOs correspond to the numeration in Fig. 8 and Fig. 9.

$24 \mu\text{m}$ fluxes of the sources from *Spitzer*-MIPS image. Using the conversion factor of $24 \mu\text{m}$ flux (7.17 Jy) toward its zero magnitude (Engelbracht et al. 2007), we calculated the $24 \mu\text{m}$ magnitudes. The SED-fitting tool developed by Robitaille et al. (2007) is available online⁸. We used this tool to fit the SED of all YSO candidates and selected the SED best-fit models according to the condition $\chi^2 - \chi_{best}^2 \text{ per datapoint} < 3$, where χ_{best}^2 is the χ^2 of the YSO best-fit model. Finally, we obtained the magnitudes of 24 sources and fitted their SED; the fitting results are listed in Table 3. Fig. 10 shows the SED of these sources. Here we used the $(J-H)$ vs. $(H-K)$ color-color diagram from 2MASS to derive the visual extinction of those sources; the values are between 3 and 35 mag. Most of the values exceed 10 mag. According to Neckel & Klare (1980), the visual extinction toward

⁸ <http://caravan.astro.wisc.edu/protostars/>

Please give a shorter version with: \authorrunning and/or \titilerunning prior to \maketitle

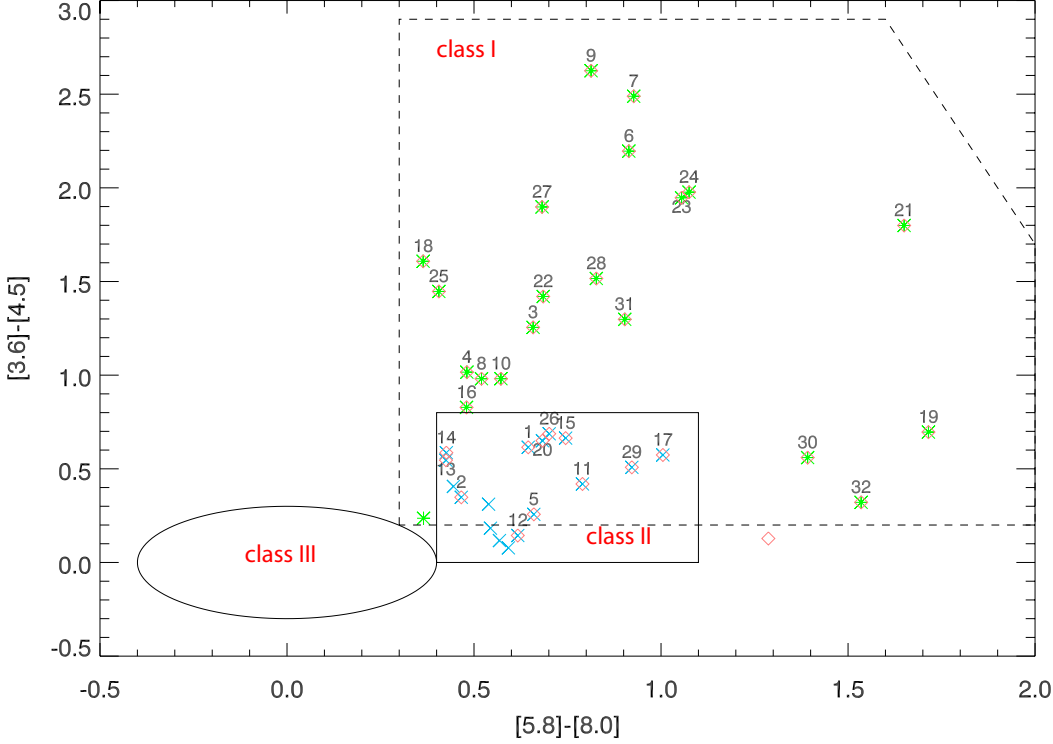


Fig. 8. GLIMPSE color-color diagram $[5.8]-[8.0]$ versus $[3.6]-[4.5]$ for sources within a circle of 4.5 in radius centered at N22. We only considered sources with detection in the four *Spitzer*-IRAC bands. The regions indicate the stellar evolutionary stage (green star = class I, blue crossing = class II) as defined by Allen et al. (2004) with the color criterion of $m_{4.5} - m_{8.0} > 1$ (red diamonds).

star-forming regions generally exceeds 10 magnitudes. Finally, we obtained the extinction between 10 and 35 mag.

The SED fitting allows us to obtain the physical parameters of the sources: the central source mass M_{\star} , the disk mass M_{disk} , the envelope mass M_{env} , and the envelope accretion rate \dot{M}_{env} . According to these parameters, Robitaille et al. (2006) classified YSOs into three stages: stage 0/I objects have significant infalling envelopes and possibly disks, they have $\dot{M}_{\text{env}}/M_{\star} > 10^{-6} \text{ yr}^{-1}$; stage II objects have optically thick disks (and possible remains of a tenuous infalling envelope), they have $M_{\text{disk}}/M_{\star} > 10^{-6}$ and $\dot{M}_{\text{env}}/M_{\star} < 10^{-6} \text{ yr}^{-1}$; and stage III objects have optically thin disks, they have $M_{\text{disk}}/M_{\star} < 10^{-6}$ and $\dot{M}_{\text{env}}/M_{\star} < 10^{-6} \text{ yr}^{-1}$. From the SEDs of the sources (see Fig. 10), we found that YSO-3, 25 and 30 are stage II objects, YSO-4, 22 and 24 could be stage I and II objects, and we suggest that the remaining 18 sources are mainly stage I sources. We have to note that due to the absence of longer wavelengths data, the results of the stage I sources may have some uncertainty.

We also found six FIS-AKARI point sources around N22, whose fluxes are listed in Cols. 3-6 of Table 4. Here, we used the Robitaille on-line tool to fit the FIS-AKARI point source fluxes by specifying 'monochromatic' instead of 'broad/narrow-band'. We did not fit source 2, because only two bands are detected. Finally, the SED fitting of the five FIS-AKARI sources indicates that they are all stage 0/I objects with masses ranging from 6.1 to $14.7 M_{\odot}$, their ages are about $10^3 \sim 10^5$ yr (see Table 5). Fig. 11 shows the SEDs of the five FIS-AKARI sources.

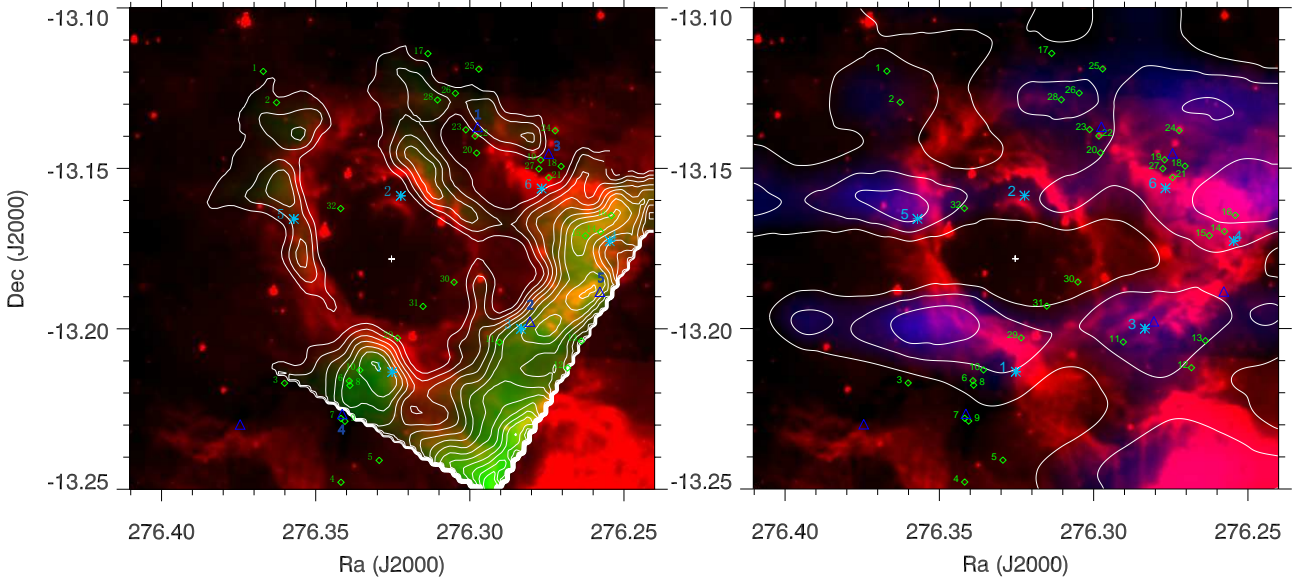


Fig. 9. Left: The background and contours are similar to Fig. 4. Right: The background and contours are similar to Fig. 6. The 32 sources of *Spitzer*-IRAC are symbolized with green diamonds. The blue stars are FIS-AKARI point sources, and triangles are BOLOCAM sources. The white plus is the center of N22.

Table 4. The fluxes for the six FIS-AKARI point sources

Source	Name	S 65 (Jy)	S 90 (Jy)	S 140 (Jy)	S 160 (Jy)
1	1825180-131240	142.3	132.6	360.0	291.0
2	1825174-130920	231.5	90.7		
3	1825080-131151	125.4	73.8		125.6
4	1825011-131012	290.0	182.8	531.7	431.5
5	1825257-130946	79.9	97.5	246.6	687.0
6	1825064-130912	226.5	170.2	488.9	721.5

Notes. The numbers of the YSOs (FIS-AKARI point sources) correspond to the numeration in Fig. 9.

Table 5. Parameters derived from the SED fitting of five YSOs (FIS-AKARI point sources)

source	χ^2_{best}/N	n	M_{\star} (M_{\odot})	Age (yr)	M_{disk} (M_{\odot})	M_{env} (M_{\odot})	\dot{M}_{env} (M_{\odot}/yr)	stage
1	18.66	1	14.7	3.2×10^3	3.0×10^{-2}	4.4×10^3	7.2×10^{-3}	0/I
3	338.00	2	6.1- 6.6	$1.9 \times 10^4 - 1.0 \times 10^5$	$8.7 \times 10^{-4} - 1.9 \times 10^{-3}$	$5.1 \times 10^1 - 7.1 \times 10^1$	$5.6 \times 10^{-4} - 2.2 \times 10^{-3}$	0/I
4	32.38	6	11.4-11.4	$4.4 \times 10^3 - 4.4 \times 10^3$	$2.3 \times 10^{-1} - 2.3 \times 10^{-1}$	$3.7 \times 10^3 - 3.7 \times 10^3$	$5.4 \times 10^{-3} - 5.4 \times 10^{-3}$	0/I
5	10.96	63	6.4-11.3	$1.3 \times 10^3 - 1.1 \times 10^5$	0.0 - 1.3	$2.0 \times 10^2 - 1.3 \times 10^3$	$5.3 \times 10^{-4} - 2.1 \times 10^{-3}$	0/I
6	8.99	29	10.7-14.0	$2.0 \times 10^3 - 3.9 \times 10^4$	0.0 - 3.1×10^{-1}	$1.3 \times 10^3 - 3.7 \times 10^3$	$2.5 \times 10^{-3} - 5.4 \times 10^{-3}$	0/I

Notes. The numbers of the YSOs (FIS-AKARI point sources) correspond to the numeration in Fig. 9.

Most of the 24 sources and the five FIS-AKARI point sources lie close to the dense cores and the active region around the N22 (see Fig. 9). Thus star formation is indeed active around N22. The formation of these YSOs may have been triggered by the expanding H II region.

From Fig. 9 (*left*), the five BOLOCAM sources can be seen across the borders of N22. Considering the gas-to-dust ratio of 100 (Enoch et al. 2006), we estimated the BOLOCAM source

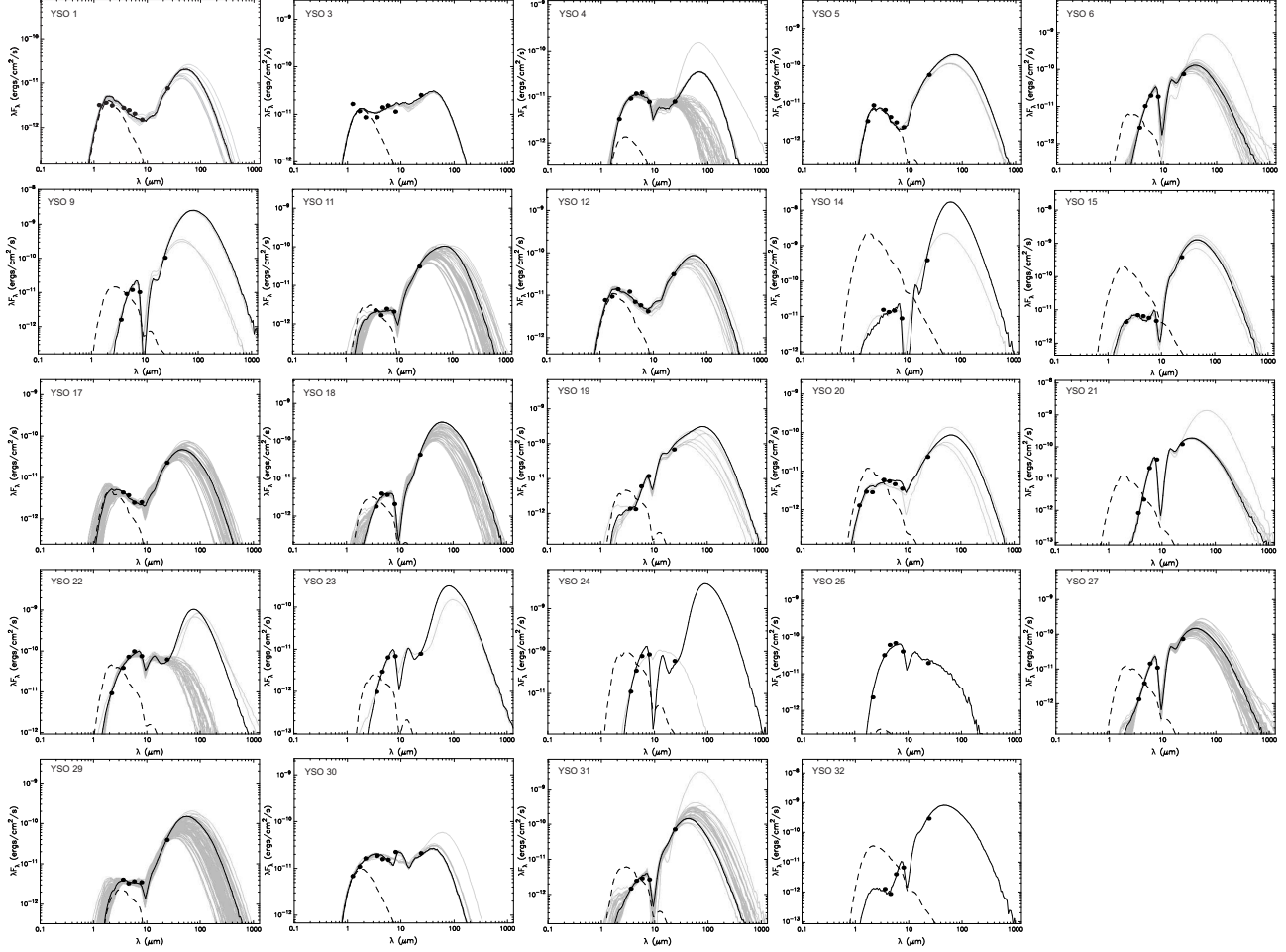


Fig. 10. SED of sources from which we obtained fluxes at $24 \mu\text{m}$ from the MIPS image. The sources are numbered according to Figs. 8 and 9. In each panel, the black line shows the best fit, and the gray lines show subsequent good fits. The dashed line shows the stellar photosphere corresponding to the central source of the best-fitting model, as it would look without circumstellar dust. The points are the input fluxes.

masses following the method of Rosolowsky et al. (2010):

$$M = \frac{13.1}{100} \left(\frac{D}{1 \text{ kpc}} \right)^2 \left(\frac{S_v}{1 \text{ Jy}} \right) \left[\frac{\exp(13.0 \text{ K}/T) - 1}{\exp(13.0/20) - 1} \right] [M_\odot],$$

where S_v is the total flux density of the BOLOCAM source in the catalog, dust temperature $T = 20$ K and distance $D = 4.1$ kpc. We obtained dust masses of the five BOLOCAM source (#1 to #5) of $7.1 M_\odot$, $0.8 M_\odot$, $18.7 M_\odot$, $7.7 M_\odot$, and $0.4 M_\odot$, respectively.

5. Collect-and-collapse scenario ?

We estimated the age of the H II region and the fragmentation time to examine whether the "collect-and-collapse" mechanism is responsible for the star formation around the bubble N22.

To obtain the age of the H II region, we used the model described by Dyson & Williams (1980) with a given radius R as

$$t(R) = \frac{4 R_s}{7 c_s} \left[\left(\frac{R}{R_s} \right)^{7/4} - 1 \right],$$

Please give a shorter version with: \authorrunning and/or \titilerunning prior to \maketitle

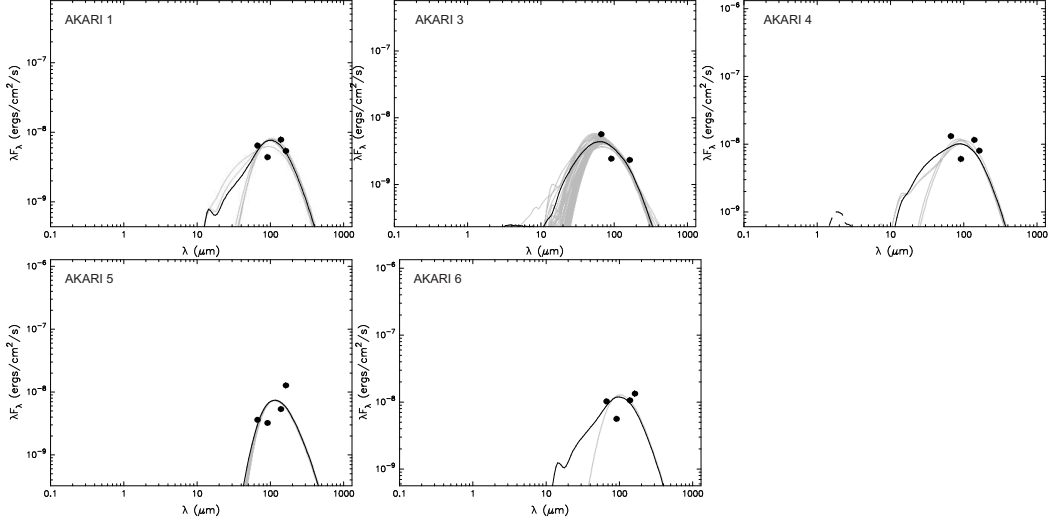


Fig. 11. SED of sources from the five FIS-AKARI sources around N22. The sources are numbered according to Table 5.

where c_s is the sound velocity in the ionized gas ($c_s=10 \text{ km s}^{-1}$) and R_s is the radius of the Strömberg sphere given by $R_s = (3N_{\text{Ly}\alpha}/4\pi n_0^2 \alpha_B)^{1/3}$, where $N_{\text{Ly}\alpha}$ is the number of ionizing photons emitted by the star per second, n_0 is the original ambient density, and $\alpha_B=2.6 \times 10^{-13} \text{ cm}^3 \text{ s}^{-1}$ is the hydrogen recombination coefficient to all levels above the ground level. Here we adopted a Lyman continuum photon flux of about $4.2 \sim 9.4 \times 10^{49} \text{ ph s}^{-1}$ (the total Lyman continuum photon flux of exciting stars, #1, #4, #7, #10, and #13, see Sec. 4.3), a radius of $\sim 1.77 \text{ pc}$, and an original ambient density of $\sim 1.0 \times 10^3 \text{ cm}^{-3}$. Finally, we derived a dynamical age of between 0.06 and 0.15 Myr for N22. To roughly estimate the original ambient density, we distributed the total mass of most dense cores, $\sim 1.2 \times 10^4 M_\odot$ (exclude core 1 and core 4), over a sphere with a radius of 2 pc.

As mentioned above, several pieces of evidence indicate that the expansion of N22 collects the gas at its periphery. To determine whether the fragmentation could occur around N22, we estimated the fragmentation time of the collected layer according to the theoretical models of Whitworth et al. (1994b):

$$t_{\text{fragment}} = 1.56 \left(\frac{\alpha_s}{0.2} \right)^{7/11} \left(\frac{N_{\text{Ly}\alpha}}{10^{49}} \right)^{-1/11} \left(\frac{n_0}{10^3} \right)^{-5/11} [\text{Myr}].$$

Using a turbulent velocity α_s ranging between 0.2 and 0.6 km s^{-1} (Whitworth et al. 1994b), we find that the fragmentation of the collected layer should occur between 1.36 and 2.93 Myr after its formation, which is later than the dynamical age. The fragmentation time is inferred by considering the uncertainty in the total Lyman continuum photon flux and turbulent velocity. Hence, the "collect-and-collapse" mechanism seems not to be responsible for the star formation activities around N22. Other processes such as the radiation-driven compression of pre-existing dense clumps (Deharveng et al. 2010) may operate here. From Figs. 1 (right) and 9 (left), we state that the compression of pre-existing dense clumps should be taking place mainly at the borders of IRDC-A and IRDC-B, which are interacting with N22. The YSOs (YSO-6, 7, 8, 9, 10, and AKARI-1) related to the IRDC-B are very likely formed by this process.

6. Summary

Using multiwavelength surveys and archival data, we have studied the ISM around the bubble N22. The main results can be summarized as follows:

(1) The PAH emission around N22 is detected at $8\ \mu\text{m}$ and the radius is about 1.77 pc. The $24\ \mu\text{m}$ emission reveals hot dust in the interior of the H II region. The 20 cm emission is bounded by $8\ \mu\text{m}$ emission and shows a shell morphology. The 20 cm emission is distributed mainly toward the north of the shell with two peaks. A cavity can be clearly seen at 20 cm emission, which may be created by the exciting-star(s) of N22.

(2) A molecular shell composed of several clumps is distributed around the H II region. Among the clumps, core 1 and core 4 are associated with IRDC-A and IRDC-B, which appear as dark extinction features against the Galactic background at mid-infrared wavelengths. The molecular shell has a total mass of about $21\ 000\ M_{\odot}$.

(3) The integrated KOSMA ^{12}CO line intensity ratios $R_{I_{\text{CO}(3-2)}/I_{\text{CO}(2-1)}}$ around N22 are measured at between 0.7 and 1.14. The higher line ratios (higher than 0.8) imply that shocks have driven into the MCs, this suggest that the expanding H II region is interacting with the surrounding MCs.

(4) We found 11 O-type star inside the H II region, five of which are located in projection inside the cavity of the 20 cm radio continuum emission. We suggest that the five O-type stars may be a cluster exciting the bubble N22.

(5) We discovered 24 YSOs that are very likely embedded in the molecular shell. Of these three YSOs are stage I-II objects, three YSOs are stage-II objects, and 18 YSOs are suggested to stage-I objects. Most of these 24 YSOs lie close to the dense cores and the active regions around the N22. We suggest that the formation of these YSOs are probably be triggered by the expanding H II region.

(6) We also fitted the SED of five FIS-AKARI point sources that are located close to the dense cores. They are all massive stars in stage 0/I.

(7) By comparing the dynamical age of N22 and the fragmentation time of the molecular shell surrounding N22, we suggest that the triggered star formation mechanism "radiation-driven compression of pre-existing dense clumps" may work here. We state that IRDC-A and IRDC-B, which are the pre-existing dense clumps, are interacting with N22, and conclude that the YSOs related to the IRDC-B are very likely formed by this process.

Acknowledgments

This work was funded by The National Natural Science Foundation of China under grant 10778703 and was partly supported by China Ministry of Science and Technology under State Key Development Program for Basic Research (2012CB821800) and The National Natural Science Foundation of China under grant 10873025.

References

- Aguirre, J., et al. 2011, ApJS, 192, 4A
Allen, L. E., Calvet, N., DAlessio, P., et al. 2004, ApJS, 154, 363
Beaumont, C.N., Williams, J.P. 2010, ApJ, 709, 791
Benjamin, R.A., Churchwell, E., Babler, B.L., et al. 2003, PASP, 115, 953

Please give a shorter version with: \authorrunning and/or \titilerunning prior to \maketitle

Bonnarel, F., Fernique, P., Bienayme, O., et al. 2000, A&AS, 143, 33B
Buckle, J.V., et al. 2010, MNRAS, 401, 204
Carey, S. J., et al. 2005, BAAS, 37, 1252
Churchwell, E., Povich, M. S., Allen, D., et al. 2006, ApJ, 649, 759
Churchwell, E., Watson, D.F., Povich, M.G., et al. 2007, ApJ, 670, 428
Condon, J. J., Cotton, W. D., Greisen, E.W., et al. 1998, AJ, 115, 1693
Deharveng, L., Zavagno, A., Caplan, J. 2005, A&A, 433, 565
Deharveng L. et al., 2010, A&A, 523, A6
Dyson, J. E., & Williams, D. A. 1980, Physics of the interstellar medium (New York: Halsted Press), 204
Elmegreen, B.G., & Lada, C.J. 1977, ApJ 214, 725
Elmegreen, B.G. 1998, in ASP Conf. Ser. 148, ed. C.E. Woodward, J.M. Schull, & H.A. Tronson, 150
Engelbracht, C. W., et al. 2007, PASP, 119 ,994
Enoch, M.L., et al. 2006, ApJ, 638, 293
Fazio, G.G., Hora, J.L., Allen, L.E., et al. 2004, ApJS, 154, 10
Guesten, R., Serabyn, E., Kasemann, C., et al. 1993, ApJ, 402, 537
Jackson, J. M., Rathborne, J. M., Shah, R. Y., et al. 2006, ApJS, 163, 145
Kolpak, M. A., Jackson, J. M., Bania, T. M., et al. 2003, ApJ, 582, 756
Martins, F., Schaerer, D., Hillier, D.J. 2005, A&A, 436, 1049
Martins, F., & Plez, B. 2006, A&A, 457, 637
Murakami et al. 2007, PASJ, 59S, 369M
Neckel, T., & Klare, G. 1980, A&AS, 42, 251
Peretto N., Fuller G.A. 2009, A&A, 505, 405
Petriella, A., Paron, S., & Giacani, E. 2010, A&A, 513, A44
Pomarès, M., Zavagno, A. et al. 2009, A&A, 494, 987
Rieke, G. H., & Lebofsky, M. J. 1985, ApJ, 288, 618
Rieke, G. H., et al. 2004, ApJS, 154, 25
Robitaille, T. P., Whitney, B. A., Indebetouw, R., et al. 2006, ApJS, 167, 256
Robitaille, T. P., Whitney, B. A., Indebetouw, R., et al. 2007, ApJS, 169, 328
Robitaille, T. P., Meade, M.R., Babler, B.L. et al. 2008, AJ, 136, 2413
Rosolowsky, E., et al. 2010, ApJS, 188, 123
Sanders, D. B., et al. 1993, in AIP Conf. Ser. 278, Back to the Galaxy, ed. S. S. Holt & F. Verter (Melville, NY: AIP), 311
Shetty R., Glover, S. C. , Dullemond, C. P., et al. 2011, MNRAS, 412, 1686
Simon R., Jackson J.M., Rathborne J.M., et al. 2006, ApJ, 639, 227S
Smith, H., et al. 2008, Proc. SPIE, 7020, 70200Z1
Watson, C., Povich, M.S., Churchwell, E.B., et al. 2008, ApJ, 681, 1341
Werner, M. W., Roellig, T. L., Low, F. J., et al. 2004, ApJS, 154, 1
Whitworth, A.P., Bhattal, A.S., Chapman, M.J., et al. 1994, MNRAS, 268, 291
Xu, J., Wang, J., & Miller, M. 2011, ApJ, 727, 81
Yamamura, I., Makiuti, S., Ikeda, N., et al. 2010, VizieR Online Data Catalog, 2298, 0
Zavagno, A., Pomars, M., Deharveng, L., et al. 2007, A&A, 472, 835
Zavagno, A., Anderson, L. D. , Russeil, D., et al. 2010, A&A, 518, L101

List of Objects

‘N22’ on page 3